Reduced-dimensional perovskite enabled by organic diamine for efficient photovoltaics

Niu, Tingting; Ren, Hui; Wu, Bo; Xia, Yingdong; Xie, Xiaoji; Yang, Yingguo; Gao, Xingyu; Chen, Yonghua; Huang, Wei

2019

Reduced-Dimensional Perovskite Enabled by Organic Diamine for Efficient Photovoltaics

Tingting Niu,[†,∇] Hui Ren,[†,∇] Bo Wu,[‡,∇] Yingdong Xia,*[†] Xiaoji Xie,[†] Yingguo Yang,[§] Xingyu Gao,[§] Yonghua Chen,*[†] and Wei Huang[†,⊥,#]

[†]Key Laboratory of Flexible Electronics (KLOFE) and Institute of Advanced Materials (IAM), Jiangsu National Synergistic Innovation Center for Advanced Materials (SICAM), Nanjing Tech University (NanjingTech), 30 South Puzhu Road, Nanjing 211816, P. R. China

[‡]Division of Physics and Applied Physics, School of Physical and Mathematical Sciences, Nanyang Technological University (NTU), 21 Nanyang Link, 637371 Singapore

[§]Shanghai Synchrotron Radiation Facility, Shanghai Institute of Applied Physics, Chinese Academy of Sciences, Shanghai 201204, P. R. China

[⊥]Shaanxi Institute of Flexible Electronics (SIFE), Northwestern Polytechnical University (NPU), 127 West Youyi Road, Xi'an 710072, China

[#]Key Laboratory for Organic Electronics & Information Displays (KLOEID) and Institute of Advanced Materials (IAM), Nanjing University of Posts and Telecommunications, 9 Wenyuan Road, Nanjing 210023, China

S *Supporting Information*

ABSTRACT: Reduced-dimensional (RD) perovskite solar cells (PSCs) are emerging as highly attractive alternatives to three-dimensional (3D) PSCs due to their dramatically improved environmental stability and photostability. Diamine-based RD perovskites with a single organic amine interlayer possess orderly inorganic sheets and a smaller insulation area, indicating great potential in combining high efficiency and long-term stability. Here, we report an efficient and stable RD PSC based on 1,4-butanediamine (BDA). We found that the BDA-based RD perovskite exhibits improved crystallinity, reduced trap-state densities, and enhanced charge mobility compared to those of butylamine (BA)-based RD (BA-RD) perovskite. A high power conversion efficiency of 17.91% was achieved with negligible hysteresis. Moreover, the device showed improved stability compared to those of BA-RD and 3D films and devices. The findings may inspire new developments in introducing organic diamine for efficient and stable RD PSCs.
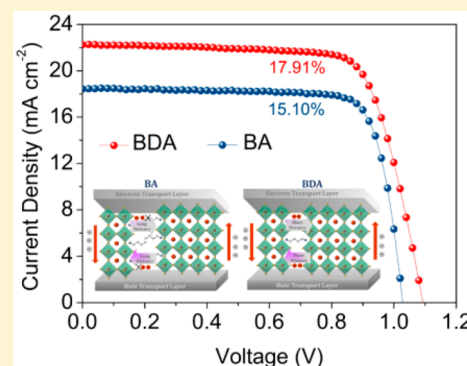
Organic−inorganic hybrid halide perovskite solar cells (PSCs) have attracted intensive attention due to their unprecedented development in power conversion efficiency (PCE) exceeding 24.2% in just a few years.[1] However, the typical three-dimensional (3D) perovskites (e.g., $CH_3NH_3PbI_3$) usually suffer from poor stability under humidity, heat, light, and oxygen.[2] Reduced-dimensional (RD) organometal halide perovskites have been shown to potentially combine high efficiency and long-term stability due to the perovskite dimension being reduced from a 3D phase to a two-dimensional (2D) phase.[3] The small organic cations (e.g., MA+, FA+, and Cs+) in the 3D structure were partly substituted by the bulkier organic ammonium cations, e.g., 2-phenylethylammonium (PEA+)[4,5] and n-butylammonium (BA+),[6,7] and the 3D perovskite structure was then tailored into a 2D layered structure due to the presence of bulkier cations, where an inorganic layer of a corner-sharing PbX6[4−] octahedral sheet was sandwiched by bulkier organic ammonium cations.[8] The increase in the long-term stability

of 2D perovskite can be attributed to the hydrophobic nature of the bulkier cations. The introduction of an organic ammonium cation allows 2D perovskites to exhibit greatly suppressed ion migration,[9] a large formation energy,[5] and ultralow self-doping.[10]

The special bulkier organic amine employed in RD perovskites have a strong influence on the overall properties,[11−16] which can be classified on the basis of differently structured RD perovskites:[17,18] (a) monoamine, e.g., PEA[19] and BA,[4,6] (b) diamine, e.g., 1,4-butanediamine (BDA) and 1,3-propanediamine (PDA),[20−22] and (c) guanidine (GA).[23] The RD perovskites are dominated by monoamine, commonly being Ruddlesden−Popper (RP) phases with the a structural formula of $(R-NH_3)_2(MA)_{n-1}Pb_nX_{3n+1}$, where pairs of interdigitated interlayer $(R-NH_3)^+$ are between inorganic
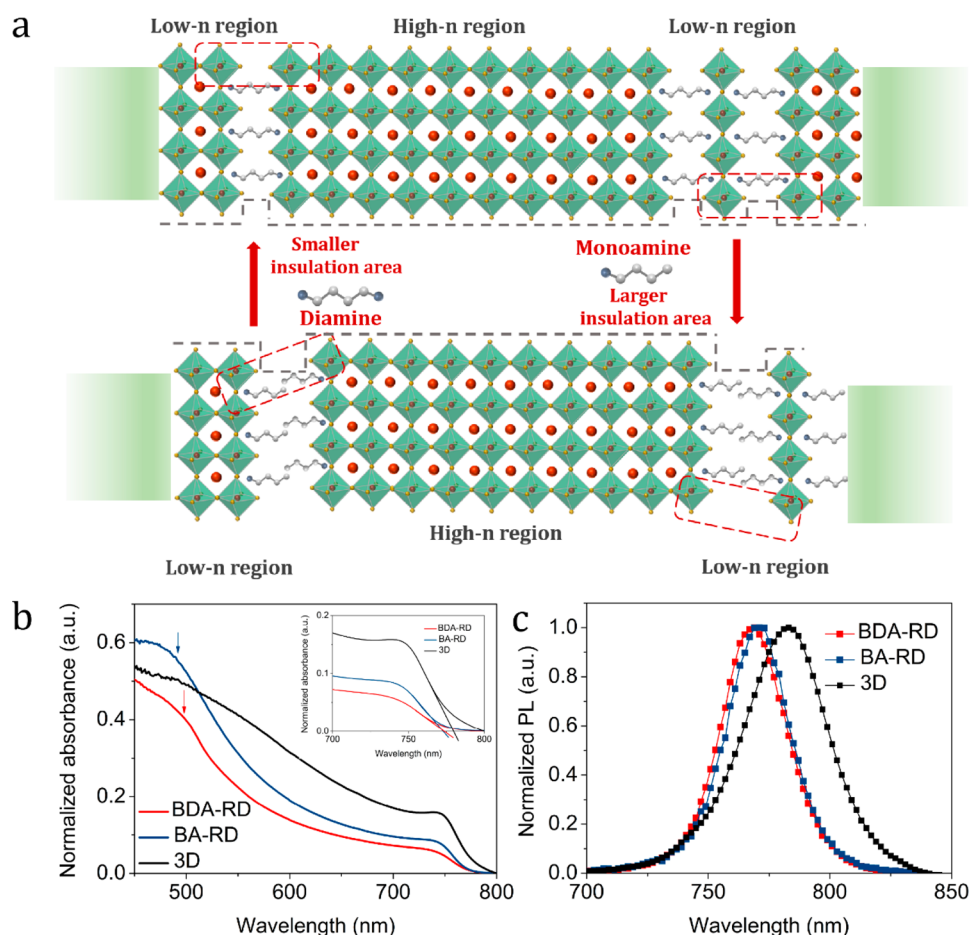
Figure 1. RD perovskite structure and optoelectronics. (a) Schematic representation of BDA-RD and BA-RD perovskites. (b) Absorption spectra of BDA-RD, BA-RD, and 3D perovskites. (c) PL spectra of BDA-RD, BA-RD, and 3D perovskites.

sheets.[6,7] The less implemented diamine is the Dion–Jacobson (DJ) phase with a structural formula of $(NH_3\text{-}R\text{-}NH_3)$-$(MA)_{n-1}Pb_nX_{3n+1}$ and require only one $(NH_3\text{-}R\text{-}NH_3)^{2+}$ per formula unit.[11,22,24] Then, GA was reported to prepare an alternating cation in the interlayer space (ACI) phase of $(GA)(MA)_nPb_nI_{3n+1}$.[11,23] Moreover, guanidinium bromide can reduce the extent of perovskite nonradiative recombination, achieving a high V_{oc} of 1.21 V in a p-i-n device.[25]

To date, however, the most commonly used organic amines for RD perovskites are a flexible alkyl chain and a simple aromatic monoamine. For example, in recent years, a hot-casting method increased the efficiency of the BA-based RD PSCs to 12.5% with $n = 4$.[7] Then, employing 2-thiophenemethylammonium (ThMA) RD PSCs, the efficiency was improved to 15.42% with $n < 6$ by MACl-assisted crystallization.[26] As the number of inorganic sheet layers increased, Quan et al. reported a BA-based RD perovskite PSC PCE of 15.36% with $n = 60$,[5] and Yang et al. further improved the efficiency of quasi-2D (or RD) PSCs with mixed-dimensional components employing 3-bromobenzylammonium (3BBA) to 18.20%.[27] In fact, less frequently applied diamine-based RD perovskites have not only a rich configurational stereochemistry with the inorganic sheets being able to stack in an orderly arrangement but also enhanced stability due to a single $(NH_3\text{-}R\text{-}NH_3)^{2+}$ layer of elimination of the van der Waals gap in an organic spacer[11,22,28,29] and a short interlayer distance. Therefore, RD perovskites with an organic diammonium cation have great potential in combining high

efficiency and long-term stability.[30] Recently, a series of diamine-based RD PSCs have been reported, containing 3-(aminomethyl)piperidinium (3AMP) or 4-(aminomethyl)-piperidinium (4AMP) cations for RD PSCs with $n = 4$, with a PCE of 7.32%;[11] 1,4-phenylenedimethanammonium (PDMA) as a spacer group for FA-based RD perovskite solar cells gave an efficiency of 7.11% with $n = 4$.[24] PDA-based RD PSCs yield a PCE of 13.0% with $n = 4$,[21] and this PSC efficiency was further improved to 13.3% with $n = 4$ showing ultrahigh stability.[22] However, compared to the monoamine-based RD PSCs, the diamine-based series regretfully showed poor efficiency.

Here, we demonstrate that 1,4-butanediamine iodide $(BDAI_2)$-based RD PSCs can exhibit a competitive PCE and stability compared to those of reported monoamine-based RD PSCs. The single-layer BDA, inducing a shorter inorganic sheet distance and orderly inorganic sheets, enabled the RD perovskite films to exhibit a high charge mobility, a low trap density, and a near single-crystalline crystal. The best-performing RD PSC exhibited a PCE of 17.91% with negligible hysteresis. The PSCs also exhibited excellent stability with an 84% initial PCE tested in ambient air without any encapsulation. Note that the RD perovskite films were prepared by a simple one-step method in ambient air irrespective of the humidity (20–80%). This prominent result is sufficient for the compound to compete with current champion RD PSCs using BA and PEA organic monoamine.
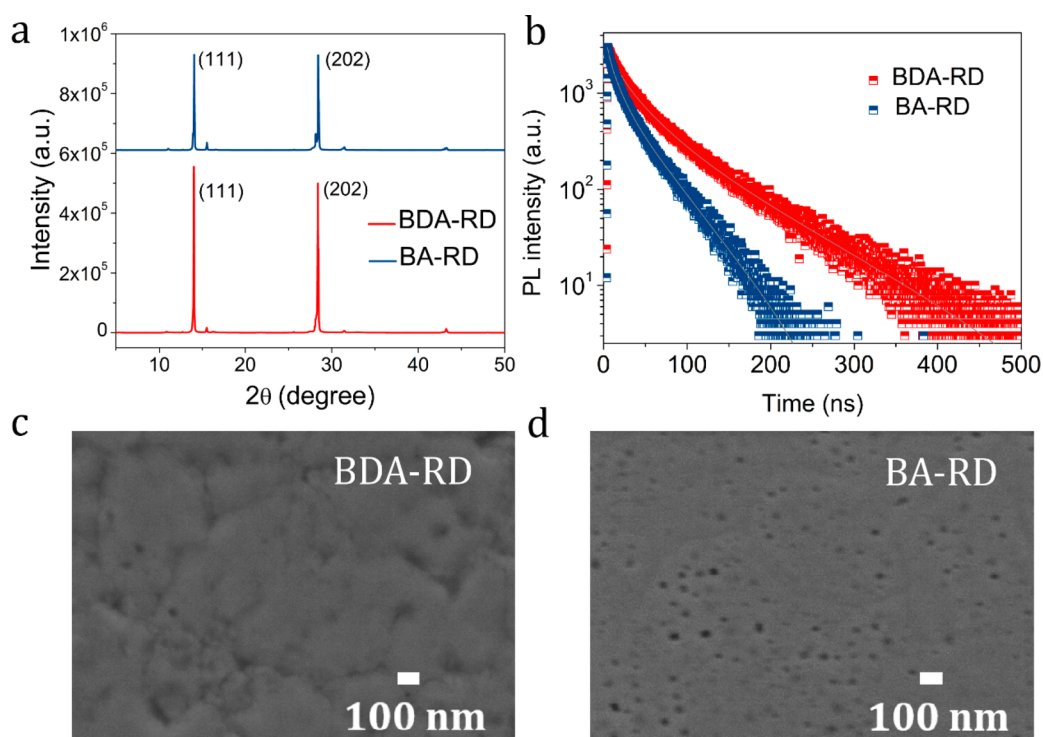
Figure 2. Characterizations of RD perovskites. (a) XRD diffraction patterns of BDA-RD and BA-RD perovskites. (b) TRPL spectra for bare BDA-RD and BA-RD perovskites. (c) SEM image for BDA-RD. (d) SEM image for BA-RD.

This work may open an avenue for organic diamine application in RD perovskites for highly efficient and stable PSCs.

The RD perovskite precursor solutions are synthesized by introducing BAI/BDAI$_2$, MACl, and PbI$_2$ according to structural formula BDAMA$_{n-1}$Pb$_n$X$_{3n+1}$ ($n = 5$)/(BA)$_2$MA$_{n-1}$Pb$_n$X$_{3n+1}$ ($n = 5$) (see the experimental section for details). The most common BA-based RD (BA-RD) perovskite consists of two layers of interacting BA, while the BDA-based RD (BDA-RD) perovskite comprises only a single BDA interlayer between the inorganic sheets (Figure 1a).[17,18] The feature of a single organic interlayer spacer in BDA-RD perovskite predominantly determines a series of prominent photoelectric properties.[11] The single organic interlayer has less disorder, which induces an orderly arrangement of inorganic sheets. In contrast, a double organic cation interlayer interacting with the van der Waals gap exerts a flexible stack, which induces an disorderly arrangement of inorganic sheets (red square in Figure 1a).[11,22] In addition, a single BDA interlayer significantly possesses an insulation area smaller than that of the double BA interlayer in RD perovskite.[11,21] The distances from the adjacent 2I to the connecting organic amine are calculated to be 4.18 and 7.27 Å for BDA-RD and BA-RD perovskites, respectively.[6,20,21] These features of BDA-RD will produce effective charge transport and a high-quality crystal.

To analyze the two structures of n (the number of inorganic octahedron layers) distribution, the optical characteristics of BDA-RD and BA-RD were first investigated by ultraviolet visible (UV−vis) (Figure 1b) and photoluminescence (PL) spectra (Figure 1c). As the UV−vis and PL data show in panels b and c of Figure 1, respectively, the spectra of BDA-RD and BA-RD appeared to be similar, which pointed to a similar n-distribution feature in each system. Furthermore, as opposed to the 3D form, we can observe a broad and misty absorption edge near 500 nm, which is similar to that of BDA-2D and BA-

2D ($n = 1$). The result might be due to the small number formation of the 2D structure; we speculate such a low-n structure may contain $n = 1$ or $n = 2$ components.[5,27,31,32] A low-n region will be beneficial for ambient stability considering the dense distribution of hydrophobic alkyl chains.[5] Notably, the preparation of a 3D perovskite film is fully consistent with that of RD perovskite. In the range of 750−800 nm, the blue-shifted sharp absorption edge with respect to the 3D form confirmed formation of a quasi-2D (or more 3D) structure, which demonstrated a large number of high-n structures were formed, which may contain $n = 10$−40 components.[5,33] Due to the smaller insulation area, the structure of the BDA-RD high-n region will tend to "more 3D" structure, which will contribute to better charge transfer performance in a high-n region of BDA-RD.[5,11,34] The results reflect the fact that our RD perovskite structure consists of a high-n structure doping low-n component (Figure 1a). Similarly, the PL spectra of BDA-RD and BA-RD appeared to exhibit a clear blue-shift of ~10 nm with respect to 3D PL (Figure 1c). No small wavelength emission peak in the PL spectrum can be explained by fast energy transfer from a doping low-n region to a high-n region, inducing the emergence of a large absorption peak.[35−38]

We investigated the crystallinity of the BDA-RD and BA-RD perovskite films using X-ray diffraction (XRD) (Figure 2a). Two dominant planes were observed at diffraction angles of 14.11° and 28.44°, representing the (111) and (202) crystallographic planes, respectively, which indicate that both RD perovskite films possess favorable crystallinity and an oriented crystal structure.[7,26,27] However, compared to BA-RD, BDA-RD has a dramatically stronger diffraction peak intensity and more pure diffraction peaks of (111) and (202), which suggest that the crystallinity of BDA-RD is superior to that of BA-RD.[13,37] The large enhancement of XRD intensity can be attributed to a regular inorganic sheet stacking in BDA-RD
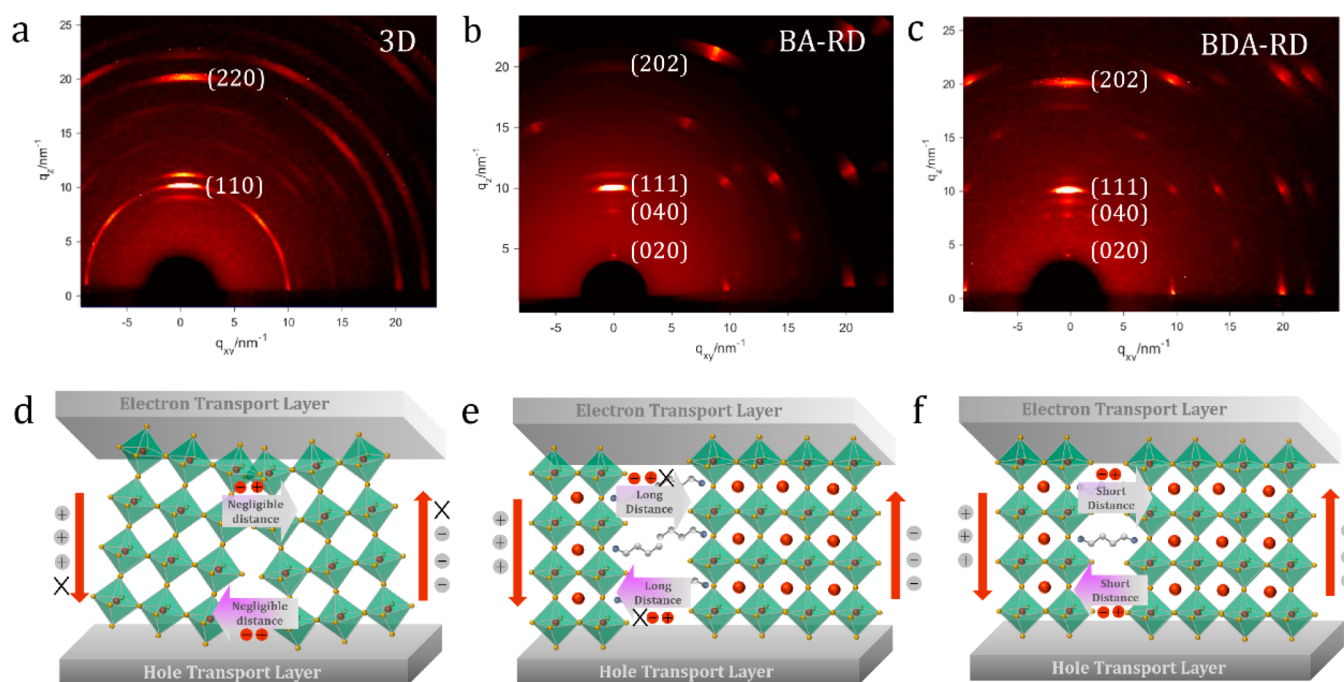
Figure 3. GIWAXS images and charge transport diagrams. (a) GIWAXS map for 3D perovskite, prepared by the same approach as RD perovskites. (b) GIWAXS map for BA-RD. (c) GIWAXS map for BDA-RD. Charge transport diagrams of (d) 3D perovskite, (e) BA-RD perovskite, and (f) BDA-RD perovskite.

perovskite (Figure 1a). Time-resolved PL (TRPL) was used to study the kinetics of excitons and free carriers in BDA-RD and BA-RD perovskite films (Figure 2b).[21,26] The sample is bare RD perovskite deposited on a quartz substrate. The TRPL profiles were fitted to the exponential decay, by which we estimated carrier average lifetimes of BDA-RD and BA-RD of 57.80 and 29.94 ns, respectively.[26,39] The enhanced lifetime of BDA-RD suggested a reduced level of nonradiative recombination associated with a lower defect density, which will facilitate effective carrier transport.[21,26,39–41] We further studied the impact of monoamine BA and diamine BDA on the morphology of films using scanning electron microscopy (SEM). An expected finding is that, as shown in panels c and d of Figure 2, the BA-RD film presents severe dips on the grains; in contrast, the BDA-RD film has almost no dips on the grains with sizes ranging from 100 to 1000 nm. To confirm the morphology of the two films, we show larger-area SEM images of BDA-RD and BA-RD in Figure S1. As one can clearly see, BDA-RD is more compact and shows a no dip surface morphology over a wide range, confirming the enhanced crystallinity, which is consistent with the XRD results.[26] The dense film avoids the contact between the hole and electron transport layer, laying the foundation for high-performance devices.[42–44]

To further investigate the RD perovskite structure and growth orientation with respect to the substrate, we performed grazing incidence wide-angle X-ray scattering (GIWAXS) analysis. The GIWAXS of 3D perovskite was also prepared for comparison. As one can clearly see in Figure 3a, the 3D film exhibited stronger intensity diffraction rings along certain extended arc segments, indicating a random crystal orientation.[7,26,45] On the contrary, the sharp and discrete Bragg spots along the same rings in both RD perovskites can be observed in panels b and c of Figure 3, which demonstrated an ordered crystal orientation.[7,26,45] The phenomenon suggests that the

bulkier organic amine effectively hinders the growth within the planar PbX_6^{4+} and MA^+, indicating that vertically oriented crystal growth is easier after the introduction of an organic amine.[6] In the GIWAXS patterns for BDA-RD and BA-RD, the diffraction spots representing the (111) and (202) planes of the orthorhombic structure of BDA-RD were stronger than those of BA-RD, which is highly consistent with the XRD pattern (Figure 2a), affirming a single BDA interlayer contributes to a more orderly crystal arrangement. It is worth noting that at $q < 10$ nm^{-1} of BDA-RD and BA-RD, we can observe (020) and (040) planes representing the $n = 2$ component, which affirms our RD perovskite structure consists of a high-n structure doping low-n component.[27,46] In general, GIWAXS pattern diffraction spots correspond to XRD diffraction peaks. However, we cannot observe XRD diffraction peaks of (020) and (040) (Figure 2a), which is due to much higher intensity (111) and (202) peaks. Therefore, the ordinate y-axis of the XRD pattern is on a log scale; the picture is shown in Figure S2. As expected, the obvious (020) and (040) diffraction peaks can be found in both RD perovskite XRD patterns, which is consistent with GIWAXS data.

To further assess the trap density and charge carrier mobility of RD-BDA and RD-BA perovskite, we measured the dark current−voltage (J_D−V) response of the electron-only and hole-only devices. As shown in Figure S3, the J_D−V curve of the blue and orange region indicates the Ohmic response of a trap-filling process. The electron and hole trap-state densities were calculated by the trap-filled limit voltage using the equation[47]

$$N_t = \frac{2\varepsilon_0 \varepsilon_r V_{TFL}}{qL^2}$$

where V_{TFL} is the onset voltage of the trap-filled limit region, ε_r is the relative dielectric constant ($\varepsilon_r = 25$), ε_0 is the vacuum
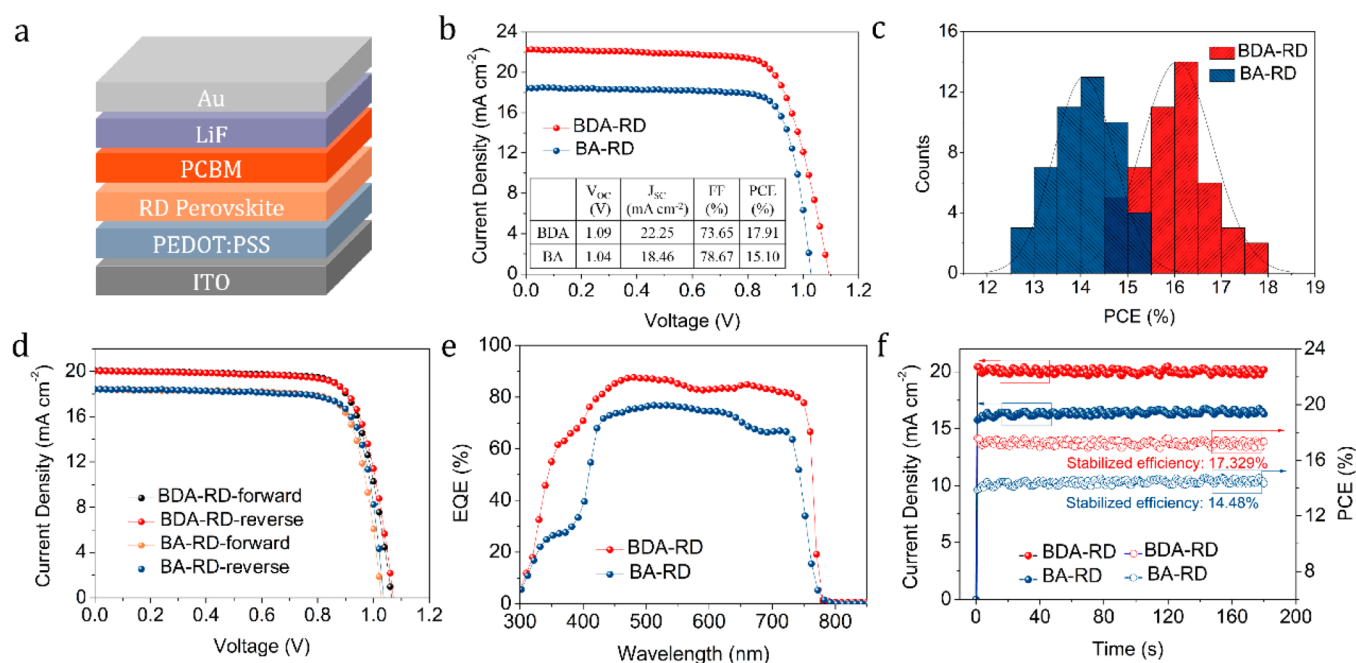
Figure 4. Device structure and performance measured under 100 mW cm^{-2} AM1.5G illumination of BDA-RD and BA-RD PSCs. (a) Device structure. (b) $J-V$ characteristics of the best device. (c) Histogram of PCEs of 48 measured devices, fitted with a Gaussian distribution (black line). (d) $J-V$ curves of BDA-RD and BA-RD PSCs under different scanning directions. (e) EQEs of the best BDA-RD and BA-RD devices. (f) Stabilized current density and power output of BDA-RD and BA-RD PSCs.

permittivity, L is the thickness of RD perovskite films, and q is the elemental charge. As shown in Figure S3, the BDA-RD film demonstrated electron and hole trap densities higher than those of the BA-RD film. The result is mainly attributed to improved crystallinity and no pinhole surface of the BDA-RD film with a regular inorganic sheet arrangement. The traps are actually the nonradiative recombination centers, which lead to deterioration of the resulting photovoltaic performance. Therefore, the low-trap density film is indispensable for the further enhancement of the performance of RD PSCs. In the trap-free space charge limit current (SCLC) regime (green region in Figure S3), the electron and hole mobilities can be estimated via the Mott–Gurney law:[47]

$$J_D = \frac{9\varepsilon\varepsilon_r\mu V_b^2}{8L^3}$$

where V_b and J_D are the applied voltage and applied current, respectively. The calculation results show that BDA-RD perovskite possesses more balanced and higher electron and hole mobilities of 1.14×10^{-3} and 1.67×10^{-3} cm^2 V^{-1} s^{-1}, respectively, compared to those of BA-RD (1.21×10^{-4} and 1.41×10^{-6} cm^2 V^{-1} s^{-1}, respectively). The effective charge transfer of BDA-RD perovskite is due to not only improved crystallinity and better film quality but also a shortened organic amine layer distance, which reduces the negative impact of insulation on charge transfer.[17,48] To better understand the effect of a shortened insulation distance on charge transfer, we simulate the charge transport diagrams of 3D, BA-RD, and BDA-RD in panels c–e of Figure 3, respectively. As shown in Figure 3c, although the lateral charge transfer of the 3D perovskite is not impeded by the insulating interlayer, the disordered crystal orientation hinders vertical charge transport. Note that oriented RD perovskites present effective vertical charge transport channels but hindered lateral charge transport by the insulted area. However, the smaller insulation area of

BDA-RD has a smaller barrier on the lateral charge transport, and we can consider that BDA-RD perovskite is similar to 3D perovskite with a vertical crystal orientation, which will contribute to faster and more efficient charge transport.

Having found evidence of RD perovskite thin films with excellent crystallinity and photophysical properties, we move on to fabricate plane heterojunction solar cells with poly(3,4-ethylenedioxythiophene) poly(styrenesulfonate) (PEDOT:PSS) and [6,6]-phenyl-C61-butyric acid methyl ester (PCBM) as charge extraction layers. The specific device structure can be seen in Figure 4a. Current density and voltage ($J-V$) curves of the optimized BDA-RD and BA-RD devices are shown in Figure 4b, in which the highest PCE of a BDA-RD device reached 17.91% with a V_{oc} of 1.09 V, a J_{sc} of 22.25 mA cm^{-2}, and a fill factor (FF) of 73.65%, while a PCE of 15.10% with a V_{oc} of 1.04 V, a J_{sc} of 18.46 mA cm^{-2}, and a FF of 78.67% was achieved with the BA-RD device. Compared to those of previously reported diamine-based RD perovskite PSCs (Table S1), we achieved the highest PCE. This can be attributed to the improved crystallinity and efficient charge transport of BDA-RD perovskite. The external quantum efficiency (EQE) is compared in Figure 4e, matched well with absorption spectra. The integrated current from the EQE spectrum yielded net current densities of 21.03 and 17.28 mA cm^{-2} of BDA-RD and BA-RD, respectively, in good agreement with the J_{sc} obtained from devices. In addition, the PCEs of both RD PSCs were also consistent with that acquired from the steady-state power output measurements by controlling the voltage at the maximum power point shown in Figure 4f. For comparison, our devices achieved V_{oc} values higher than those of usual PEDOT:PSS-based devices, such as the V_{oc} of 1.01 eV reported for BA-based devices ($n = 4$) with a parallel device structure,[7] attributed to the lower level of nonradiative recombination in films.[26] This illustrates that BDA-RD perovskites show a promising improvement in V_{oc} and could

be allowed to have great potential as the top cell in a tandem solar cell.[49] Moreover, our results indicate that high-performance BDA-RD PSCs can be repeatedly fabricated using a simple and effective annealing-assisted solution process (AASP) method, which keeps a constant substrate temperature during the solution processing. The basic steps for preparing perovskite films are schematically described in Figure S4. Note that the device performance is strongly associated with the substrate temperature (Figure S5 and Table S2), the annealing temperature (Figure S6 and Table S3), and the precursor concentration (Figure S7 and Table S4).[50] The PCE distribution of the devices using BDA-RD and BA-RD perovskite is compared in Figure 4c, and the V_{oc}, J_{sc}, and FF distributions of both devices are shown in Figure S8, which demonstrate excellent reproducibility with an average PCE of >16% for BDA-RD and >14% for BA-RD. Interestingly, the efficiencies of both RD PSCs are even higher than that of 3D PSC with the same preparation methods (Figure S9), which might be due to oriented crystal growth effectively facilitating the extraction of charge in the transport layer.

Moreover, as presented in Figure 4d, both RD PSCs exhibited negligible hysteresis light $J-V$ curves with different scanning directions, indicating that the efficiencies measured for our RD PSCs with stable $J-V$ curves are reliable. One possible reason is the fullerene PCBMs interact with mobile ions in perovskite to form a fullerene halide radical,[51] which can stabilize electrostatic properties, reducing the electric field-induced anion migration and thus resulting in no hysteresis.[52,53] The possible contribution of the good interfaces between the perovskite films and charge-transporting layers (i.e., PEDOT:PSS and PCBM) cannot be ruled out in light of our recent report on hysteresis-free devices based on the same charge-transporting layers of PEDOT:PSS and PCBM. Another important reason may be the suppressed ion migration and self-doping in RD perovskite films.

Another favorable advantage of BDA-RD perovskites is the great stability compared to those of BA-RD and 3D perovskites. We simultaneously investigated the long-term stability of BDA-RD, BA-RD, and 3D films, all of which were exposed under ambient conditions with a relative humidity of ∼60%. As shown in Figure S10, no PbI$_2$ peak was observed in the BDA-RD perovskite film after 127 days, while the 3D and BA-RD films exhibited strong and weak PbI$_2$ peaks, respectively, after ∼110 days. It should be noted that 3D weak PbI$_2$ peaks appeared after only 35 days, which is attributed to RD perovskites being more stable to humidity than 3D perovskites, due to dense hydrophobic alkyl chains in the low-n region of RD perovskite avoiding direct contact with water in air. Another significant decomposition feature is the increased (202) shoulder peak intensity of BA-RD perovskite after 115 days, while this shoulder peak of BDA-RD perovskite is almost unchanged after 254 days (Figure S10). We also tested the long-term stability of BDA-RD, BA-RD, and 3D PSCs in ambient air without any encapsulation (Figure S11). The BDA-RD device retained 84% of its original PCE after 1182 h, while the device with BA-RD and 3D perovskites gave levels of their initial PCE of 73% after 1176 h and 39% after 1008 h. Figure S12 shows the normalized PCE, V_{oc}, J_{sc}, and FF as a function of testing time under continuous 1 sun illumination. After constant illumination for 298 h, the BDA-RD PSC retained 90% of its original PCE, while BA-RD PSC gave 73% of its initial PCE. For BDA-RD PSC, there is a significant degradation in V_{oc} or J_{sc}, while all parameters (V_{oc},

J_{sc}, and FF) for BA-RD appeared to decrease significantly. This result indicates that BDA-RD PSC has not only better humidity stability than BA-RD PSC but also better continuous illumination stability. The stability decreased in the following order: BDA-RD > BA-RD > 3D perovskite. The low-n region of RD perovskite, including high-density organic amine, can effectively resist water in air and suppress ion migration, which induce improved stability for RD perovskite compared to that of 3D perovskite. Moreover, the fact that the BDA-RD perovskite films and corresponding solar cells were more stable than the BA-RD perovskite can be attributed to the following. (1) There is an unstable van der Waals gap between BA in BA-RD perovskite, while no such gap exists in BDA-RD perovskites. (2) BDA-RD perovskite exhibited improved crystallinity, inducing the more compact and stable crystal structure. (3) BDA-RD perovskite has a density of defect states lower than that of BA-RD perovskite and is less likely to be in contact with ambient air.

In summary, we demonstrated a highly efficient RD PSC with a single organic amine interlayer by employing BDA as the bulkier organic cation. The high-quality films of BDA-RD perovskite with improved crystallinity and low trap density can be obtained by a simple one-step method in ambient air irrespective of the humidity (20−80%). The fabricated BDA-RD perovskites remarkably improve crystallinity, reduce trap density, and facilitate charge transport. The excellent crystallinity and charge transfer performance yield significant enhancements in PCE from 15.10% (BA-RD) to 17.91% (BDA-RD) as well as markedly improved stability. The merits of high efficiency and great stability, together with the solution processability and fabrication in ambient air irrespective of humidity, promote the application of organic diamine in RD perovskites for real products.

■ ASSOCIATED CONTENT

ⓢ Supporting Information

The Supporting Information is available free of charge on the ACS Publications website at DOI: 10.1021/acs.jpclett.9b00750.

> Experimental methods, SEM images, XRD patterns, characteristic $J-V$ trace of electron-only and hole-only devices, schematic illustration of the AASP method, $J-V$ characteristics, histogram of device performance parameters, and stability tests (PDF)

■ AUTHOR INFORMATION

Corresponding Authors
*E-mail: iamydxia@njtech.edu.cn.
*E-mail: iamyhchen@njtech.edu.cn.
ORCID ⓘ
Yingdong Xia: 0000-0003-4023-3231
Xiaoji Xie: 0000-0002-4830-1246
Yingguo Yang: 0000-0002-1749-2799
Xingyu Gao: 0000-0003-1477-0092
Yonghua Chen: 0000-0002-9694-4246
Author Contributions
∇T.N., H.R., and B.W. contributed equally to this work.
Notes
The authors declare no competing financial interest.

■ ACKNOWLEDGMENTS

■ REFERENCES

(1) NREL. Best Research Cell Efficiency Chart. https://www.nrel.gov/pv/assets/pdfs/best-research-cell-efficiencies-190416.pdf (accessed April 16, 2019).

(2) Wang, Z.; Shi, Z.; Li, T.; Chen, Y.; Huang, W. Stability of Perovskite Solar Cells: A Prospective on the Substitution of the A Cation and X Anion. *Angew. Chem., Int. Ed.* **2017**, *56*, 1190−1212.

(3) Zhang, X.; Ren, X.; Liu, B.; Munir, R.; Zhu, X.; Yang, D.; Li, J.; Liu, Y.; Smilgies, D. M.; Li, R.; et al. Stable High Efficiency Two-Dimensional Perovskite Solar Cells via Cesium Doping. *Energy Environ. Sci.* **2017**, *10*, 2095−2102.

(4) Smith, I. C.; Hoke, E. T.; Solis-Ibarra, D.; McGehee, M. D.; Karunadasa, H. I. A Layered Hybrid Perovskite Solar-Cell Absorber with Enhanced Moisture Stability. *Angew. Chem., Int. Ed.* **2014**, *53*, 11232−11235.

(5) Quan, L. N.; Yuan, M.; Comin, R.; Voznyy, O.; Beauregard, E. M.; Hoogland, S.; Buin, A.; Kirmani, A. R.; Zhao, K.; Amassian, A.; et al. Ligand-Stabilized Reduced-Dimensionality Perovskites. *J. Am. Chem. Soc.* **2016**, *138*, 2649−2655.

(6) Cao, D. H.; Stoumpos, C. C.; Farha, O. K.; Hupp, J. T.; Kanatzidis, M. G. 2D Homologous Perovskites as Light-Absorbing Materials for Solar Cell Applications. *J. Am. Chem. Soc.* **2015**, *137*, 7843−7850.

(7) Tsai, H.; Nie, W.; Blancon, J. C.; Stoumpos, C. C.; Asadpour, R.; Harutyunyan, B.; Neukirch, A. J.; Verduzco, R.; Crochet, J. J.; Tretiak, S.; et al. High-Efficiency Two-Dimensional Ruddlesden-Popper Perovskite Solar Cells. *Nature* **2016**, *536*, 312−316.

(8) Mitzi, D. B. Templating and Structural Engineering in Organic−Inorganic Perovskites. *J. Chem. Soc. Dalton. Trans.* **2001**, *1*, 1−12.

(9) Lin, Y.; Bai, Y.; Fang, Y.; Wang, Q.; Deng, Y.; Huang, J. Suppressed Ion Migration in Low-Dimensional Perovskites. *ACS Energy Lett.* **2017**, *2*, 1571−1572.

(10) Peng, W.; Yin, J.; Ho, K. T.; Ouellette, O.; De Bastiani, M.; Murali, B.; El Tall, O.; Shen, C.; Miao, X.; Pan, J.; Alarousu, E.; He, J.-H.; Ooi, B. S.; Mohammed, O. F.; Sargent, E.; Bakr, O. M. Ultralow Self-Doping in Two-Dimensional Hybrid Perovskite Single Crystals. *Nano Lett.* **2017**, *17*, 4759−4767.

(11) Mao, L.; Ke, W.; Pedesseau, L.; Wu, Y.; Katan, C.; Even, J.; Wasielewski, M. R.; Stoumpos, C. C.; Kanatzidis, M. G. Hybrid Dion-Jacobson 2D Lead Iodide Perovskites. *J. Am. Chem. Soc.* **2018**, *140*, 3775−3783.

(12) Proppe, A. H.; Quintero-Bermudez, R.; Tan, H.; Voznyy, O.; Kelley, S. O.; Sargent, E. H. Synthetic Control over Quantum Well Width Distribution and Carrier Migration in Low-Dimensional Perovskite Photovoltaics. *J. Am. Chem. Soc.* **2018**, *140*, 2890−2896.

(13) Zheng, H.; Liu, G.; Zhu, L.; Ye, J.; Zhang, X.; Alsaedi, A.; Hayat, T.; Pan, X.; Dai, S. The Effect of Hydrophobicity of Ammonium Salts on Stability of Quasi-2D Perovskite Materials in Moist Condition. *Adv. Energy Mater.* **2018**, *8*, 1800051.

(14) Giorgi, G.; Yamashita, K.; Palummo, M. Nature of the Electronic and Optical Excitations of Ruddlesden−Popper Hybrid Organic−Inorganic Perovskites: The Role of the Many-Body Interactions. *J. Phys. Chem. Lett.* **2018**, *9*, 5891−5896.

(15) Liu, X.; Zhang, N.; Tang, B.; Li, M.; Zhang, Y.; Yu, Z.; Gong, H. Highly Stable New Organic−Inorganic Hybrid 3D Perovskite CH$_3$NH$_3$PdI$_3$ and 2D Perovskite (CH$_3$NH$_3$)$_3$Pd$_2$I$_7$: DFT Analysis, Synthesis, Structure, Transition Behavior, and Physical Properties. *J. Phys. Chem. Lett.* **2018**, *9*, 5862−5872.

(16) Quarti, C.; Marchal, N.; Beljonne, D. Tuning the Optoelectronic Properties of Two-Dimensional Hybrid Perovskite Semiconductors with Alkyl Chain Spacers. *J. Phys. Chem. Lett.* **2018**, *9*, 3416−3424.

(17) Cheng, Z.; Lin, J. Layered Organic−Inorganic Hybrid Perovskites: Structure, Optical Properties, Film Preparation, Patterning and Templating Engineering. *CrystEngComm* **2010**, *12*, 2646−2662.

(18) Liang, C.; Zhao, D.; Li, Y.; Li, X.; Peng, S.; Shao, G.; Xing, G. Ruddlesden−Popper Perovskite for Stable Solar Cells. *Energy Environ. Mater.* **2018**, *1*, 221−231.

(19) Chen, H.; Xia, Y.; Wu, B.; Liu, F.; Niu, T.; Chao, L.; Xing, G.; Sum, T.; Chen, Y.; Huang, W. Critical Role of Chloride in Organic Ammonium Spacer on the Performance of Low-Dimensional Ruddlesden-Popper Perovskite Solar Cells. *Nano Energy* **2019**, *56*, 373.

(20) Safdari, M.; Svensson, P. H.; Hoang, M. T.; Oh, I.; Kloo, L.; Gardner, J. M. Layered 2D Alkyldiammonium Lead Iodide Perovskites: Synthesis, Characterization, and Use in Solar Cells. *J. Mater. Chem. A* **2016**, *4*, 15638−15646.

(21) Ma, C.; Shen, D.; Ng, T. W.; Lo, M. F.; Lee, C. S. 2D Perovskites with Short Interlayer Distance for High-Performance Solar Cell Application. *Adv. Mater.* **2018**, *30*, 1800710.

(22) Ahmad, S.; Fu, P.; Yu, S.; Yang, Q.; Liu, X.; Wang, X.; Wang, X.; Guo, X.; Li, C. Dion-Jacobson Phase 2D Layered Perovskites for Solar Cells with Ultrahigh Stability. *Joule* **2019**, *3*, 889−890.

(23) Soe, C. M. M.; Stoumpos, C. C.; Kepenekian, M.; Traore, B.; Tsai, H.; Nie, W.; Wang, B.; Katan, C.; Seshadri, R.; et al. New Type of 2D Perovskites with Alternating Cations in the Interlayer Space, (C(NH$_2$)$_3$)(CH$_3$NH$_3$)$_n$Pb$_n$I$_{3n+1}$: Structure, Properties, and Photovoltaic Performance. *J. Am. Chem. Soc.* **2017**, *139*, 16297−16309.

(24) Li, Y.; Milic, J. V.; Ummadisingu, A.; Seo, J. Y.; Im, J. H.; Kim, H. S.; Liu, Y.; Dar, M. I.; Zakeeruddin, S. M.; Wang, P.; Hagfeldt, A.; Grätzel, M. Bifunctional Organic Spacers for Formamidinium-Based Hybrid Dion-Jacobson Two-Dimensional Perovskite Solar Cells. *Nano Lett.* **2019**, *19*, 150−157.

(25) Luo, D.; Yang, W.; Wang, Z.; Sadhanala, A.; Hu, Q.; Su, R.; Shivanna, R.; Trindade, G. F.; Watts, J. F.; Xu, Z.; et al. Enhanced Photovoltage for Inverted Planar Heterojunction Perovskite Solar Cells. *Science* **2018**, *360*, 1442−1446.

(26) Lai, H.; Kan, B.; Liu, T.; Zheng, N.; Xie, Z.; Zhou, T.; Wan, X.; Zhang, X.; Liu, Y.; Chen, Y. Two-Dimensional Ruddlesden−Popper Perovskite with Nanorodlike Morphology for Solar Cells with Efficiency Exceeding 15%. *J. Am. Chem. Soc.* **2018**, *140*, 11639−11646.

(27) Yang, R.; Li, R.; Cao, Y.; Wei, Y.; Miao, Y.; Tan, W. L.; Jiao, X.; Chen, H.; Zhang, L.; Chen, Q.; et al. Oriented Quasi-2D Perovskites for High Performance Optoelectronic Devices. *Adv. Mater.* **2018**, *30*, 1804771.

(28) Liu, B.; Long, M.; Cai, M.; Yang, J. Two-Dimensional van der Waals Heterostructures Constructed via Perovskite (C$_4$H$_9$NH$_3$)$_2$XBr$_4$ and Black Phosphorus. *J. Phys. Chem. Lett.* **2018**, *9*, 4822−4827.

(29) Chen, Z.; Wang, Y.; Sun, X.; Xiang, Y.; Hu, Y.; Jiang, J.; Feng, J.; Sun, Y.; Wang, X.; Wang, G.; et al. Remote Phononic Effects in Epitaxial Ruddlesden−Popper Halide Perovskites. *J. Phys. Chem. Lett.* **2018**, *9*, 6676−6682.

(30) Chen, Y.; Yu, S.; Sun, Y.; Liang, Z. Phase Engineering in Quasi-2D Ruddlesden−Popper Perovskites. *J. Phys. Chem. Lett.* **2018**, *9*, 2627−2631.

(31) Koh, T. M.; Shanmugam, V.; Schlipf, J.; Oesinghaus, L.; Müller-Buschbaum, P.; Ramakrishnan, N.; Swamy, V.; Mathews, N.; Boix, P. P.; Mhaisalkar, S. G. Nanostructuring Mixed-Dimensional Perovskites: A Route toward Tunable, Efficient Photovoltaics. *Adv. Mater.* **2016**, *28*, 3653−3661.

(32) Zhang, Y.; Wang, R.; Li, Y.; Wang, Z.; Hu, S.; Yan, X.; Zhai, Y.; Zhang, C.; Sheng, C. Optical Properties of Two-Dimensional

Perovskite Films of $(C_6H_5C_2H_4NH_3)_2[PbI_4]$ and $(C_6H_5C_2H_4NH_3)_2(CH_3NH_3)_2[Pb_3I_{10}]$. *J. Phys. Chem. Lett.* **2019**, *10*, 13−19.

(33) Jiang, Y.; Yuan, J.; Ni, Y.; Yang, J.; Wang, Y.; Jiu, T.; Yuan, M.; Chen, J. Reduced-Dimensional a-CsPbX$_3$ Perovskites for Efficient and Stable Photovoltaics. *Joule* **2018**, *2*, 1356−1368.

(34) Xing, G.; Wu, B.; Wu, X.; Li, M.; Du, B.; Wei, Q.; Guo, J.; Yeow, E. K. L.; Sum, T. C.; Huang, W. Transcending the Slow Bimolecular Recombination in Lead-Halide Perovskites for Electroluminescence. *Nat. Commun.* **2017**, *8*, 14558.

(35) Wang, N.; Cheng, L.; Ge, R.; Zhang, S.; Miao, Y.; Zou, W.; Yi, C.; Sun, Y.; Cao, Y.; Yang, R.; et al. Perovskite Light-Emitting Diodes Based on Solution-Processed Self-Organized Multiple Quantum Wells. *Nat. Photonics* **2016**, *10*, 699−706.

(36) Quan, L. N.; Zhao, Y.; García de Arquer, F. P.; Sabatini, R.; Walters, G.; Voznyy, O.; Comin, R.; Li, Y.; Fan, J. Z.; Tan, H.; Pan, J.; Yuan, M.; Bakr, O. M.; Lu, Z.; Kim, D. H.; Sargent, E. H. Tailoring the Energy Landscape in Quasi-2D Halide Perovskites Enables Efficient Green-Light Emission. *Nano Lett.* **2017**, *17*, 3701−3709.

(37) Chen, Y.; Sun, Y.; Peng, J.; Zhang, W.; Su, X.; Zheng, K.; Pullerits, T.; Liang, Z. Tailoring Organic Cation of 2D Air-Stable Organometal Halide Perovskites for Highly Effcient Planar Solar Cells. *Adv. Energy. Mater.* **2017**, *7*, 1700162.

(38) Lee, J. W.; Dai, Z.; Han, T. H.; Choi, C.; Chang, S. Y.; Lee, S. J.; De Marco, N.; Zhao, H.; Sun, P.; Huang, Y.; Yang, Y. 2D Perovskite Stabilized Phase-Pure Formamidinium Perovskite Solar Cells. *Nat. Commun.* **2018**, *9*, 3021.

(39) Straus, D. B.; Kagan, C. R. Electrons, Excitons, and Phonons in Two-Dimensional Hybrid Perovskites: Connecting Structural, Optical, and Electronic Properties. *J. Phys. Chem. Lett.* **2018**, *9*, 1434−1447.

(40) Ding, J.; Lian, Z.; Li, Y.; Wang, S.; Yan, Q. The Role of Surface Defects in Photoluminescence and Decay Dynamics of HighQuality Perovskite MAPbI3 Single Crystals. *J. Phys. Chem. Lett.* **2018**, *9*, 4221−4226.

(41) Chirvony, V. S.; Martínez-Pastor, J. P. Trap-Limited Dynamics of Excited Carriers and Interpretation of the Photoluminescence Decay Kinetics in Metal Halide Perovskites. *J. Phys. Chem. Lett.* **2018**, *9*, 4955−4962.

(42) Ma, X.; Gao, W.; Yu, J.; An, Q.; Zhang, M.; Hu, Z.; Wang, J.; Tang, W.; Yang, C.; Zhang, F. Ternary Nonfullerene Polymer Solar Cells with Efficiency > 13.7% by Integrating the Advantages of the Materials and Two Binary Cells. *Energy Environ. Sci.* **2018**, *11*, 2134−2141.

(43) Zhang, M.; Gao, W.; Zhang, F.; Mi, Y.; Wang, W.; An, Q.; Wang, J.; Ma, X.; Miao, J.; Hu, Z.; et al. Efficient Ternary Non-fullerene polymer solar cells with PCE of 11.92% and FF of 76.5%. *Energy Environ. Sci.* **2018**, *11*, 841−849.

(44) Hu, Z.; Zhang, F.; An, Q.; Zhang, M.; Ma, X.; Wang, J.; Zhang, J.; Wang, J. Ternary Nonfullerene Polymer Solar Cells with a Power Conversion Efficiency of 11.6% by Inheriting the Advantages of Binary Cells. *ACS Energy Lett.* **2018**, *3*, 555−561.

(45) Chen, A. Z.; Shiu, M.; Ma, J. H.; Alpert, M. R.; Zhang, D.; Foley, B. J.; Smilgies, D. M.; Lee, S. H.; Choi, J. J. Origin of Vertical Orientation in Two-Dimensional Metal Halide Perovskites and its Effect on Photovoltaic Performance. *Nat. Commun.* **2018**, *9*, 1336.

(46) Zhang, X.; Munir, R.; Xu, Z.; Liu, Y.; Tsai, H.; Nie, W.; Li, J.; Niu, T.; Smilgies, D. M.; Kanatzidis, M. G.; et al. Phase Transition Control for High Performance Ruddlesden−Popper Perovskite Solar Cells. *Adv. Mater.* **2018**, *30*, 1707166.

(47) Dong, Q.; Fang, Y.; Shao, Y.; Mulligan, P.; Qiu, J.; Cao, L.; Huang, J. Electron-Hole Diffusion Lengths > 175 μm in Solution-Grown CH$_3$NH$_3$PbI$_3$ Single Crystals. *Science* **2015**, *347*, 967−970.

(48) Chao, L.; Niu, T.; Xia, Y.; Ran, X.; Chen, Y.; Huang, W. Efficient and Stable Low-Dimensional Ruddlesden-Popper Perovskite Solar Cells Enabled by Reducing Tunnel Barrier. *J. Phys. Chem. Lett.* **2019**, *10*, 1173−1179.

(49) Zhao, D.; Yu, Y.; Wang, C.; Liao, W.; Shrestha, N.; Grice, C.; Cimaroli, A.; Guan, L.; Ellingson, R.; Zhu, K.; et al. Low-Bandgap Mixed Tin−Lead Iodide Perovskite Absorbers with Long Carrier Lifetimes for All-Perovskite Tandem Solar Cells. *Nat. Energy.* **2017**, *2*, 17018.

(50) Chao, L.; Xia, Y.; Li, B.; Xing, G.; Chen, Y.; Huang, W. Room-Temperature Molten Salt for Facile Fabrication of Efficient and Stable Perovskite Solar Cells in Ambient Air. *Chem* **2019**, *5*, 995.

(51) Xu, J.; Buin, A.; Ip, A. H.; Li, W.; Voznyy, O.; Comin, R.; Yuan, M.; Jeon, S.; Ning, Z.; McDowell, J. J.; et al. Perovskite−Fullerene Hybrid Materials Suppress Hysteresis in Planar Diodes. *Nat. Commun.* **2015**, *6*, 7081.

(52) De Bastiani, M.; Dell'Erba, G.; Gandini, M.; D'Innocenzo, V.; Neutzner, S.; Kandada, A. R. S.; Grancini, G.; Binda, M.; Prato, M.; Ball, J. M.; Caironi, M.; Petrozza, A. Ion Migration and the Role of Preconditioning Cycles in the Stabilization of the J−V Characteristics of Inverted Hybrid Perovskite Solar Cells. *Adv. Energy Mater.* **2016**, *6*, 1501453.

(53) Shao, Y.; Xiao, Z.; Bi, C.; Yuan, Y.; Huang, J. Origin and Elimination of Photocurrent Hysteresis by Fullerene Passivation in CH$_3$NH$_3$PbI$_3$ Planar Heterojunction Solar Cells. *Nat. Commun.* **2014**, *5*, 5784.